Nanoscale Advances

ROYAL SOCIETY OF CHEMISTRY

PAPER

View Article Online
View Journal | View Issue

Cite this: *Nanoscale Adv.*, 2025, **7**, 3088

Fabricating a hexagonal FeTe monolayer with a moiré superlattice on topological insulator Bi_2Te_3

Yen-Hui Lin,[a] Yu-Hsiang Chung,[b] Guan-Yu Chen,[a] Hung-Chin Lee,[a] Nitin Kumar,[a] Chia-Ju Chen,[a] Jia-An Lin,[b] Chun-Yu Mou,[ac] Allan H. MacDonald,[d] Chih-Kang Shih,[d] Dah-An Luh,*[ef] Jung-Jung Su*[b] and Pin-Jui Hsu*[a]

The growth of a hexagonal FeTe (α-FeTe) thin layer on three-dimensional topological insulator Bi_2Te_3 has been systematically investigated by combining scanning tunneling microscopy/spectroscopy (STM/STS) with density-functional theory (DFT) calculations. Through post-annealing at 560 K after room-temperature deposition of Fe onto Bi_2Te_3, α-FeTe has been fabricated with an atomic lattice constant of 4.0 ± 0.1 Å, which is much smaller than the 4.4 ± 0.1 Å of the Te-terminated Bi_2Te_3 surface. The lattice mismatch and a sufficiently large FeTe–Bi_2Te_3 distance give rise to a moiré pattern with a periodicity of 6.0 ± 0.1 nm, corresponding to a $p(15 \times 15)$ superlattice. On the other hand, an enhanced projected density of states (PDOS) is found at about −0.8 eV and +1.4 eV of α-FeTe/Bi_2Te_3 in the tunneling spectra. These enhancements, as interpreted from the DFT calculation, arise from the contribution of the 3d out-of-plane orbitals in Fe. DFT calculations also reveal nonzero net magnetization and indicate ferromagnetic (FM) order in the system – contrasting the well-studied bicollinear antiferromagnetism in β-FeTe/Bi_2Te_3. To summarize, our successful fabrication of α-FeTe/Bi_2Te_3 provides a distinct platform from β-FeTe/Bi_2Te_3, enabling an exploration of the interplay between magnetism and interface-induced superconductivity.

Received 10th February 2025
Accepted 20th March 2025

DOI: 10.1039/d5na00136f

rsc.li/nanoscale-advances

1 Introduction

In recent years, Fe-based superconductors have received extensive attention in fundamental studies as well as technological applications due to their extraordinary electronic, magnetic and superconducting properties.[1–5] In particular, two-dimensional (2D) Fe-chalcogenides, including FeS, FeSe, FeTe and $FeTe_{1-x}Se_x$ nanostructured materials, exhibit unexpected high superconducting transition temperature (T_c), comprising a new class of high-temperature 2D superconductors. For example, although the FeSe bulk crystal has a T_c only up to 8 K,[6–8] one-unit-cell FeSe epitaxially grown on $SrTiO_3$ can reach a remarkably high T_c above 100 K.[9–13] Such interfacial-enhanced superconductivity has also been reported on FeSe/$BaTiO_3$,[14,15] FeSe/$LaFeO_3$ [16] and $FeTe_{1-x}Se_x$/$SrTiO_3$ [17,18] with an increase of T_c values higher than that of their bulk counterparts.

By exploiting molecular beam epitaxy (MBE) and chemical vapor deposition (CVD), both hexagonal (α-FeTe) and tetragonal FeTe (β-FeTe) thin films have been grown on $SrTiO_3$ [19] and SiO_2/Si[20,21] substrates. Intriguing 2D ferromagnetism with a high Curie temperature nearly about 300 K has been achieved in the α-FeTe nanosheets on SiO_2/Si as a result of lattice distortion and Stoner instability.[20,21] While the bulk compound of FeTe is non-superconducting, the β-FeTe monolayer grown on 3D topological insulator (TI) Bi_2Te_3 by contrast shows an interfacial-induced superconductivity coexisting with an antiferromagnetically ordered state,[22–25] offering a potential platform for the emergence of topological superconductivity hosting Majorana fermionic particles.[26–31] Besides β-FeTe, the growth of α-FeTe on Bi_2Te_3 remains not reported yet, which would become a fertile ground to not only study the corresponding magnetism and superconductivity, but also compare with β-FeTe/Bi_2Te_3.

In this work, we have carried out systematic studies on the growth of α-FeTe on Bi_2Te_3 by scanning tunneling microscopy/spectroscopy (STM/STS) along with density functional theory (DFT). After room-temperature deposition of Fe onto Bi_2Te_3, an α-FeTe thin layer can be formed by post-annealing at about 560 K. According to atomically-resolved topographic images, α-FeTe exhibits a lattice constant of about 4.0 ± 0.1 Å slightly larger than 3.8 ± 0.1 Å extracted from β-FeTe/Bi_2Te_3, but smaller than the 4.4 ± 0.1 Å of the Te-terminated Bi_2Te_3 surface. Interestingly, a moiré pattern with periodicity about 6.0 ± 0.1 nm

[a]*Department of Physics, National Tsing Hua University, Hsinchu 300044, Taiwan. E-mail: pinjuihsu@phys.nthu.edu.tw*

[b]*Department of Electrophysics, National Yang Ming Chiao Tung University, Hsinchu 300093, Taiwan. E-mail: jungjsu@nycu.edu.tw*

[c]*Center for Quantum Science and Technology, National Tsing Hua University, Hsinchu 300044, Taiwan*

[d]*Department of Physics, The University of Texas at Austin, Austin, Texas 78712, USA*

[e]*Department of Physics, National Central University, Taoyuan 32001, Taiwan. E-mail: luh.dah.an@gmail.com*

[f]*National Synchrotron Radiation Research Center, Hsinchu 30076, Taiwan*

appears on the α-FeTe thin layer that exhibits the same crystalline orientation symmetry with the bulk Bi_2Te_3 substrate, leading to a $p(15 \times 15)$ superlattice as a result of lattice mismatch. The larger interlayer distance required for moiré formation, as extracted from our DFT results, arises from contracting the inner bond (1.04 Å) of Fe–Te within FeTe while relaxing the FeTe–Bi_2Te_3 interlayer distance (2.13 Å). Moreover, from spin-dependent band structure calculations and tunneling spectroscopy measurements on α-FeTe/Bi_2Te_3, the out-of-plane 3d orbitals of Fe contribute to the enhanced PDOS at about −0.8 eV and +1.4 eV in tunneling dI/dU spectra. Our DFT calculations show that each Fe atom possesses a magnetic moment of 3.41 μ_B, while other atoms carry only negligible magnetic moments, the magnetic moment carried by Fe leans into the z-direction by around 36.42°, which is a comprehensive effect of the spin–orbit coupling along with crystal fields. The ferromagnetic properties of Fe are also evident in the spin-projected band structure of s_z. The majority of s_z projections are largely buried deep in the Fermi sea whereas most minority s_z projections lie near the Fermi surface.

2 Experimental and theoretical methods

2.1 Experimental details

The whole experiment was performed in an ultra-high vacuum (UHV) environment with a base pressure at about 2.0×10^{-10} mbar. The clean Bi_2Te_3 surface with tellurium (Te) termination was obtained by a low-temperature cleavage of the bulk single crystal at 80 K. Bi_2Te_3 crystals were prepared from melted materials of Bi (99.9999%) and Te (99.9999%) in a sealed quartz ampoule and subsequently cooled down slowly, resulting in the formation of a rod-shaped specimen. The as-grown crystals were cleaved easily to obtain the atomic flat sample surfaces. High purity iron (Fe) (99.9995%) was evaporated from an e-beam evaporator (FOCUS) while keeping the substrate at RT, followed by post-annealing at around 560 K (610 K) to have an α-FeTe (β-FeTe) thin layer. After the sample preparation, it was immediately transferred to the measurement chamber where a low-temperature scanning tunneling microscope (LT-STM) (UNISOKU, USM-1500), with a base temperature of 4.2 K, was employed for characterization. All topographic images were scanned in constant current mode and *in situ* tunneling conductance (dI/dU) spectra and maps were recorded with an external lock-in amplifier (Stanford Research Systems) at frequency 3991 Hz and 20 to 50 mV voltage modulation.

2.2 Theoretical computations

The density-functional theory (DFT) calculation was performed using the Vienna *Ab initio* Simulation Package (VASP) with Perdew–Burke–Ernzerhof (PBE) generalized gradient approximation (GGA). To model the system, we choose a hexagonal supercell with an in-plane lattice constant of 4.372 Å for the pure Bi_2Te_3 slab and 4.25 Å for FeTe on Bi_2Te_3. The van der Waal correction we include is DFT + D2. The cutoff energy for the wavefunction is 174.98 eV for the pure Bi_2Te_3 slab and 267.88 eV for FeTe on Bi_2Te_3. Spin–orbit coupling is included and fully relativistic pseudopotential is used in all calculations. Hubbard on-site interaction is included through GGA + U with $U = 2$ eV for the presence of iron. In obtaining the band structure and the density of states (DOS), we used a $15 \times 15 \times 1$ Monkhorst–Pack k-point grid. DOS is shown with a Gaussian smearing of 0.1 eV in energy. Since the STM measurement collects signals mainly of small in-plane momenta, we integrate, in reciprocal space, the wavefunction projection convoluted by a Gaussian function (all in reciprocal space) to obtain our projected density of states (PDOS). The Gaussian has a width of $0.4\pi/a$ and is centered at $\bar{\Gamma}$ – to highlight contributions from small momenta.

3 Results and discussion

3.1 Temperature-dependent growth of α- and β-FeTe/Bi_2Te_3

Fig. 1(a) represents the STM topographic overview of 0.65 ± 0.1 ML Fe evaporated onto the Bi_2Te_3 surface after post-annealing at 450 K, and Fe clusters with a few nanometers in size have been seen. Note that the ML defined here is deduced from the atomic density of Fe epitaxially grown on Cu(111).[32–34] It is also noted that Fig. 1(a) is similar to the Fe deposited directly on Bi_2Te_3 at RT without a post-annealing process. As the post-annealing temperature increases to 520 K, the nanometer-sized Fe clusters start decreasing in amount and developing into 2D nano-islands as indicated by the two white arrows in

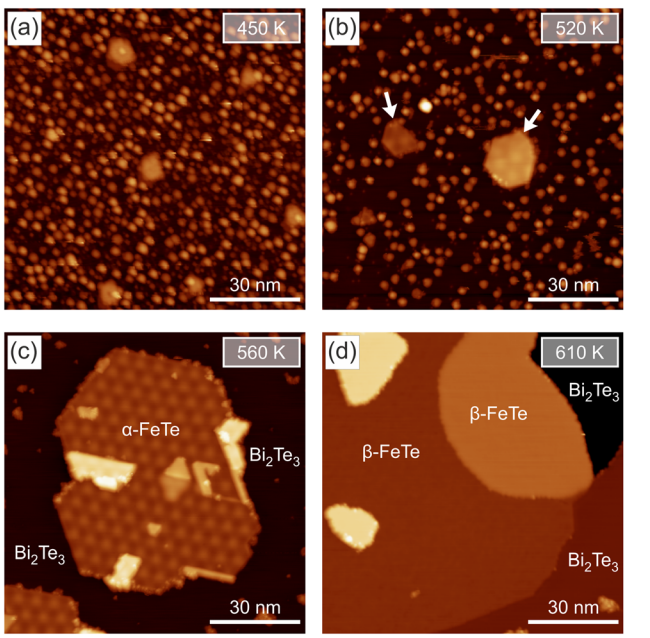

Fig. 1 (a) An overview STM image of Fe deposited onto the Bi_2Te_3 surface at RT and then post-annealed at 450 K. The surface is covered with Fe nanoclusters. (b) As the post-annealing temperature increases to 520 K, the Fe nanoclusters merged into 2D nano-islands as indicated by the two white arrows. (c) When the post-annealing temperature reaches 560 K, the α-FeTe thin layer appears with a hexagonal dot-like pattern, *i.e.*, moiré superlattice, on the surface. (d) The formation of β-FeTe films can be eventually achieved at the post-annealing temperature rising up to 610 K. (Scan parameters for all images $U_b = -1.0$ V, $I_t = 50$ pA).

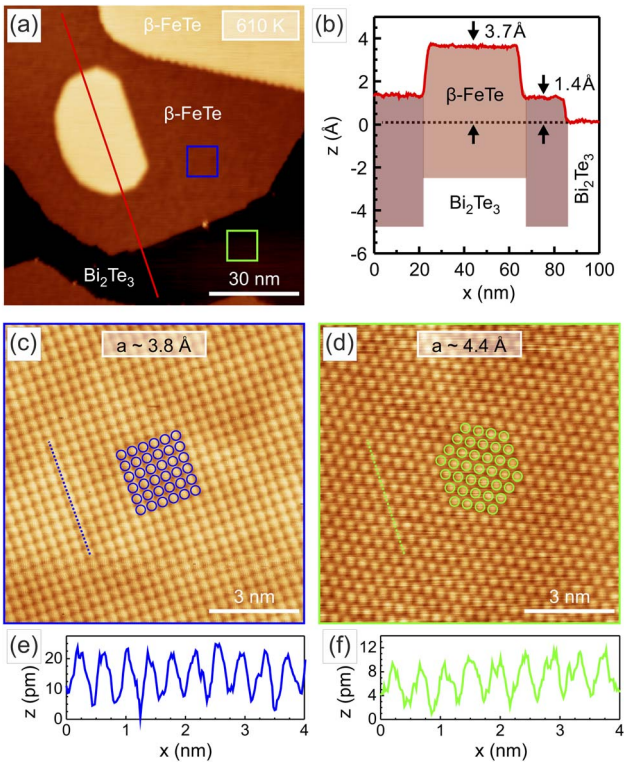

Fig. 2 (a) An overview STM image of β-FeTe/Bi_2Te_3 prepared with the post-annealing temperature at 610 K. (b) The topographic line profile, *i.e.*, taken from the red solid line from (a), across different β-FeTe atomic layers. (c) Atomic resolution image of the β-FeTe UC layer acquired from the blue square frame of (a), where the rectangular atomic lattice with a fourfold symmetry (empty blue circles) has been revealed. (d) The atomic resolution image of the Bi_2Te_3 surface has been measured from the green square frame of (a), where the hexagonal atomic lattice with a sixfold symmetry (empty green circles) has been identified. The atomic lattice constants of the β-FeTe UC layer and Bi_2Te_3 surface are about 3.8 ± 0.1 Å and 4.4 ± 0.1 Å as extracted from the topographic line profiles shown in (e) and (f), respectively. (Scan parameters for (a) $U_b = -1.0$ V, $I_t = 50$ pA, (c) $U_b = -10$ mV, $I_t = 1.0$ nA, and (d) $U_b = -10$ mV, $I_t = 1.0$ nA).

Fig. 1(b). This suggests that the reaction of Fe atoms with the Te-terminated surface of Bi_2Te_3 could begin to take place at a sufficiently high temperature. When the post-annealing temperature reaches 560 K, the α-FeTe thin layer appears with surface morphology consisting of a hexagonal dot-like pattern on top of the Bi_2Te_3 substrate as shown in Fig. 1(c). Finally, the formation of β-FeTe films can be realized at post-annealing temperature rising up to 610 K, which is in agreement with the results reported before.[24,35–38] It is worth mentioning that Fe–Bi is an immiscible system, whereas Fe–Bi nanostructures are typically metastable and amorphous without a well-defined crystalline order.[39–41]

3.2 Atomic-scale characterization of α- and β-FeTe thin films

After obtaining an overall picture of temperature-dependent growth of α-FeTe and β-FeTe on Bi_2Te_3, we further characterize these two structure phases down to the atomic scale. Fig. 2(a) displays the STM overview of β-FeTe/Bi_2Te_3 prepared at 610 K, and the corresponding line profile across different atomic layers of β-FeTe, *i.e.*, the red solid line in Fig. 2(a), has been shown in Fig. 2(b). Two apparent heights of 1.4 ± 0.1 Å and 3.7 ± 0.1 Å from β-FeTe thin layers have been extracted, which are obviously smaller than the *c*-axis lattice constant of 6.25 Å from the bulk FeTe crystal.[42] Due to the high-temperature post-annealing, an interdiffusion between deposited Fe atoms and the Te-terminated Bi_2Te_3 surface might potentially take place, leading to the formation of single-unit-cell (UC) β-FeTe that is probably embedded into the topmost quintuple layer (QL) of Bi_2Te_3 according to the observed low apparent height.[24,35–38]

The atomic resolution image of the top β-FeTe layer has been shown in Fig. 2(c), where the rectangular atomic lattice exhibits a fourfold symmetry (blue empty circles) in contrast to the hexagonal close-packed atomic lattice with a sixfold symmetry (green empty circles) in the bare Bi_2Te_3 surface of Fig. 2(d). It is worth mentioning that the surface of the β-FeTe thin layer is atomically clean and does not contain excess Fe atoms as resolved in the case of bulk FeTe,[25,43,44] suggesting that the UC layer of FeTe has a stoichiometric composition. According to the topographic line profiles plotted in Fig. 2(e) and (f), the atomic lattice constants about 3.8 ± 0.1 Å and 4.4 ± 0.1 Å have been extracted from Fig. 2(c) and (d) for the β-FeTe UC layer and Bi_2Te_3 surface, respectively, which are in line with previous studies.[24,36–38]

With a post-annealing temperature of 560 K lower than the 610 K of β-FeTe, the α-FeTe thin layer can be fabricated on Bi_2Te_3 as shown in Fig. 3(a). Note that a relatively lower growth temperature implies that α-FeTe might be a thermodynamically meta-stable state, which is similar to the growth behavior of α- and β-FeTe on the $SrTiO_3$ substrate by employing an MBE-based approach.[19] Unlike the absence of long-range ordered structures on the β-FeTe surface, intriguingly, there is a nano-scale periodic modulation constituting a hexagonal dot-like pattern on the α-FeTe surface from the overview topography in Fig. 3(a). To understand such dot-like feature, the atomic resolution image on the α-FeTe surface, *i.e.*, blue square frame of Fig. 3(a), has been obtained in Fig. 3(b), where the hexagonal atomic lattice superposed with a larger unit-cell superlattice has been revealed.

Given the resultant topographic line profiles plotted in Fig. 3(c) (black dashed line from Fig. 3(a) and (d)) (blue dashed line from Fig. 3(b)), the atomic lattice constant is about 4.0 ± 0.1 Å for the α-FeTe and the average periodicity of the large-scale superlattice is about 6.0 ± 0.1 nm, resulting in a $p(15 \times 15)$ supercell. We would like to denote that the atomic lattice constant 4.0 ± 0.1 Å extracted from α-FeTe/Bi_2Te_3 is slightly larger than the 3.8 Å of either α-FeTe thin films on $SrTiO_3$ [19] and SiO_2/Si[20,21] substrates or the corresponding bulk counterpart[45] as reported previously. Besides the lattice constant, the orientation of the atomic lattice as well as the superlattice of the α-FeTe thin layer are registered to the underlying Bi_2Te_3 substrate, which can be verified from the atomically resolved image at the edge boundary between α-FeTe and Bi_2Te_3 in Fig. 3(e) (green square frame from Fig. 3(a)). Moreover, we would also like to denote that both orientation symmetry and structural periodicity of the $p(15 \times 15)$ superlattice do not vary with the temperature based on the measurements 77 K and 4.2 K. Taking

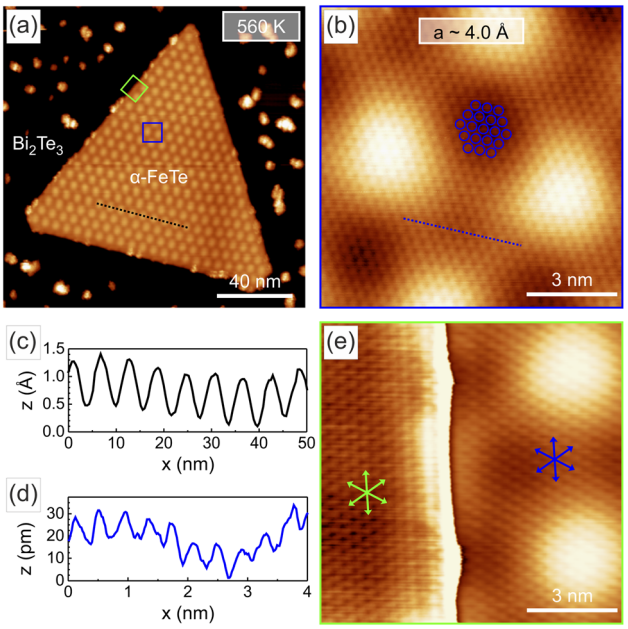

Fig. 3 (a) STM topographic overview of α-FeTe/Bi_2Te_3 fabricated at a post-annealing temperature of 560 K. (b) Atomically resolved image on the α-FeTe surface acquired from the blue square frame in (a), where the atomic lattice superposed with the moiré superlattice can be observed. (c) and (d) Topographic line profiles taken from the black (blue) dashed line from (a) and (b), where the atomic lattice constant and periodicity of the moiré superlattice of α-FeTe/Bi_2Te_3 are 4.0 ± 0.1 Å and 6.0 ± 0.1 nm, respectively. (e) Atomically resolved image at the edge boundary between α-FeTe and Bi_2Te_3 (green) square frame from (a), both the orientation symmetry of atomic lattice as well as moiré superlattice on the α-FeTe thin layer are registered to the underlying Bi_2Te_3 substrate. (Scan parameters for (a) $U_b = -1.0$ V, $I_t = 50$ pA, (b) $U_b = -10$ mV, $I_t = 1.0$ nA, and (e) $U_b = -10$ mV, $I_t = 1.0$ nA).

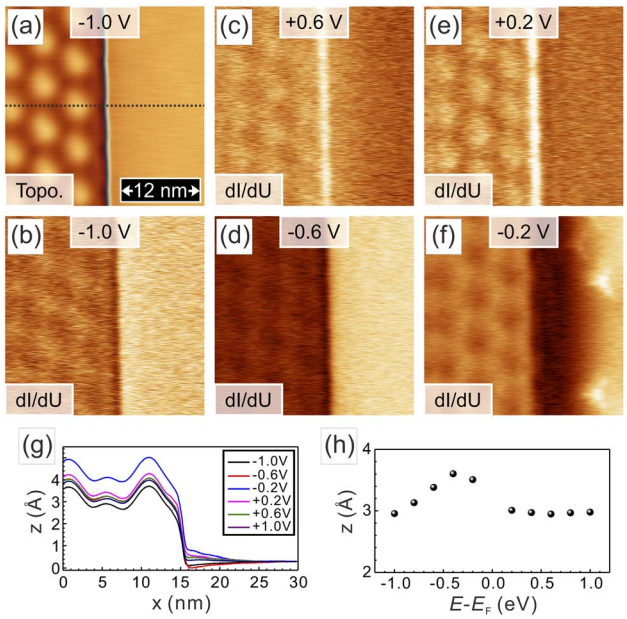

Fig. 4 (a) Zoom-in topography at the edge proximity of α-FeTe/Bi_2Te_3. The surface morphology of the moiré superlattice stays the same within the bias voltage range of ±1.0 eV. (b)–(f) Bias-dependent conductance maps reveal the local intensity of tunneling conductance spatially modulated within the moiré superlattice. (g) Bias-dependent height profiles along the black dashed line in (a) and an apparent height of 3.2 Å on average can be extracted from (h).

these observations into account, we attribute the $p(15 \times 15)$ superlattice to a typical moiré pattern as a consequence of lattice mismatch between the α-FeTe thin layer and bulk Bi_2Te_3 substrate.

Fig. 4(a) is the zoom-in topography taken at the edge proximity of α-FeTe/Bi_2Te_3, where the surface morphology of the moiré superlattice does not change with bias voltages, and it stays the same within the bias voltage range of ±1.0 eV. In contrast to bias-independent surface morphology, the local intensity of tunneling conductance is spatially modulated with the moiré superlattice as shown in the bias-dependent conductance maps arranged from Fig. 4(b)–(f). The bias-dependent topographic line profiles measured from α-FeTe to Bi_2Te_3, *i.e.*, black dashed line in Fig. 4(a), have been presented in Fig. 4(g), and the corresponding bias-dependent apparent heights are summarized in Fig. 4(h) in which an apparent height of about 3.2 Å on average has been identified from the α-FeTe thin layer atop of Bi_2Te_3.

After having atomic-scale analyses of the lattice constant, surface crystalline symmetry and apparent height, *etc.*, we could construct the simple structure model to gain further insights on the moiré superlattice of the α-FeTe thin layer on Bi_2Te_3. Fig. 5(a) illustrates the moiré superlattice under the assumption of two atomic layers overlapped with a lattice mismatch, where the orange (black) empty circle refers to Te-terminated α-FeTe (Bi_2Te_3) with a lattice constant of 4.0 Å (4.38 Å) extracted experimentally. Interestingly, this simple model reproduces the lattice symmetry of the moiré superstructure, but gives rise to a periodicity of about 4.6 nm that is shorter than 6.0 ± 0.1 nm obtained experimentally. To obtain consistent periodicity, we need to consider a smaller lattice constant of 4.28 Å, *i.e.*, an isotropic compression of about 2.3% compared to 4.38 Å, for the Te-terminated Bi_2Te_3 surface as depicted in Fig. 5(b), which might associate with structural relaxation occurring at the topmost QL of Bi_2Te_3 in order to accommodate the incorporation of the α-FeTe sublayer.

3.3 Electronic band structures and atomic-orbital-dependent PDOS

We have further performed DFT calculation in order to examine the STM measurements. Fig. 5(c) and (d) show the structure after relaxation for two atomic layers of FeTe on the Bi_2Te_3 substrate, which is the most experimentally consistent combination among all possibilities for α-FeTe on Bi_2Te_3. In particular, after a systematic study over a range of effective lattice constants (4.0 to 4.4 Å) this structure shown is the lowest energy stacking out of that at the three symmetry points in a moire lattice while using an in-plane lattice constant of 4.25 Å to be most comparable with the STM observations. The Bi_2Te_3 substrate is modeled by 3 quintuple layers. The bottom quintuple layer is fixed in all directions while the top two and the

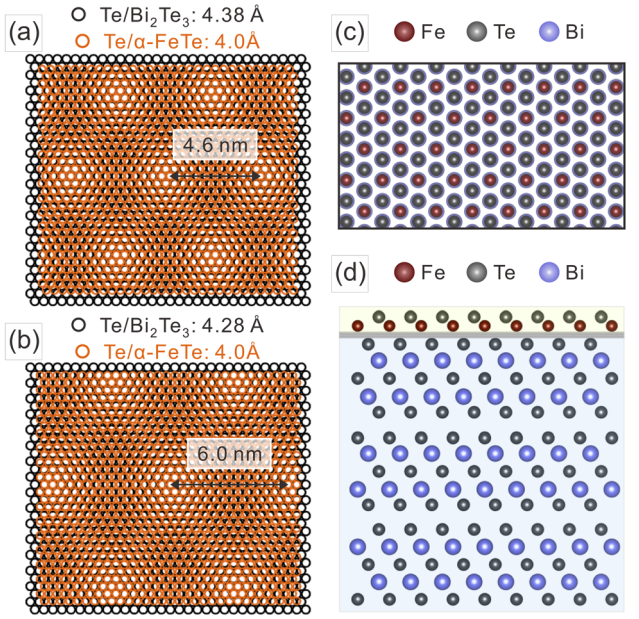

Fig. 5 (a) Moiré superlattice with a periodicity of 4.6 nm can be constructed by two atomic layers overlapped with a lattice mismatch. Orange (black) empty circle represents the Te-terminated α-FeTe (Bi_2Te_3) with a lattice constant of 4.0 Å (4.38 Å) determined experimentally. (b) Moiré superlattice with a periodicity of 6.0 nm can be obtained from the smaller lattice constant 4.28 Å of Te-terminated Bi_2Te_3. (c) and (d) Top and side views of the crystalline structure of the α-FeTe monolayer on the Bi_2Te_3 substrate from DFT relaxation calculation. A slight gap (grey shaded area) emerges between FeTe and the Bi_2Te_3 substrate that enables the formation of the moiré pattern.

FeTe layers are fully relaxed. A vacuum layer of 100 Å thickness is added on the top to account for the long range nature of van der Waal interaction. We notice that the top Fe and Te layers are bound strongly to a distance of only 1.04 Å, leaving room for a gap of 2.13 Å between the Fe layer and the Te underneath; this gap is crucial for the moiré pattern to form between the FeTe monolayer and the Bi_2Te_3 substrate. That yields a total width of FeTe, measuring from the top of the Bi_2Te_3 substrate to be 3.16 Å, which is consistent with the apparent height of 3.2 Å on average measured from STM.

Next we have performed band structure and PDOS calculations. Before going to the α-FeTe on Bi_2Te_3 setup, let us first discuss the case of the Bi_2Te_3 substrate along. Fig. 6(a) and (b) show the band structure for the top Bi and Te atomic layers in such substrate. The result here is obtained for three quintuple layers of Bi_2Te_3. The bottom quintuple layer is fixed in all directions while the top two are fully relaxed; a vacuum layer of 100 Å is also added on top of Bi_2Te_3. Our results are consistent with previous calculation which shows the signature cone-like surface state around the Fermi surface. This surface state is contributed in almost equal footing from Bi and from Te, and corresponds to the small but non-zero PDOS around the Fermi surface in Fig. 6(c). Experimental STS measurement (Fig. 6(d)) at the same time shows qualitatively the same behavior at around zero bias.

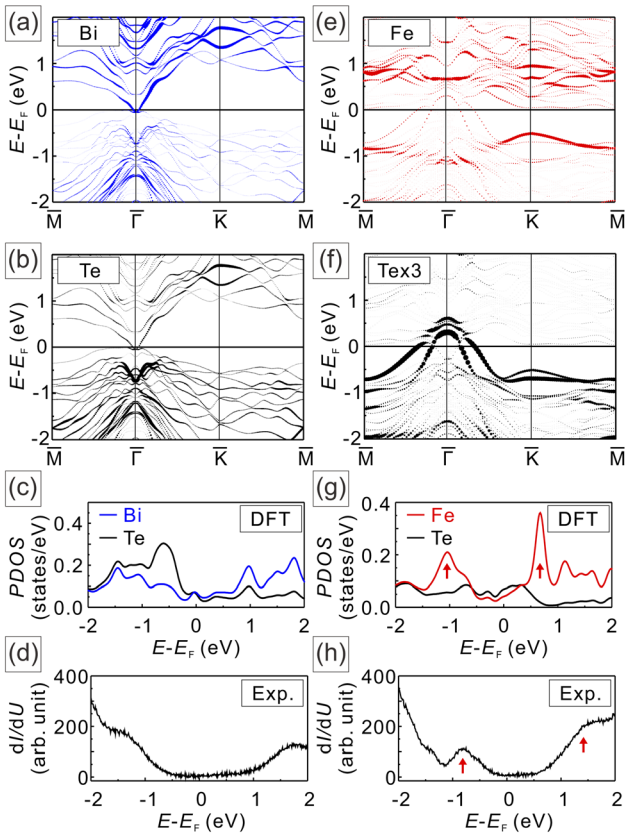

Fig. 6 (a) and (b) show the DFT-calculated band structure from the top Bi and Te atomic layers of the Bi_2Te_3 substrate, featuring the surface states at the Fermi surface. (c) The corresponding PDOS from DFT calculation exhibits non-zero but small PDOS around the Fermi surface that is also observed in experimental STS measurement of (d). (e) and (f) are the DFT-calculated band structures from the top Fe and Te atomic layers of the structure shown in Fig. 5(d). The Fe layer gives much stronger contribution around the Fermi surface and the (f) has been scaled three times larger. (g) is the PDOS from the same structure featuring local maxima (indicated by red arrows) above and below the Fermi surface from the Fe layer. (h) is the tunneling d*I*/d*U* curve that shows the corresponding enhanced PDOS (also indicated by red arrows). (Stabilization parameters for (d) and (h) $U_b = +2.0$ V, $I_t = 1.0$ nA).

For the case of α-FeTe on Bi_2Te_3, the band structure and PDOS have been calculated based on the structure shown in Fig. 5(d). Fig. 6(e) and (f) are the band structures for the top Fe and Te atomic layers of α-FeTe/Bi_2Te_3, respectively. In the vicinity of the Fermi surface, the contribution from Fe dominates over that from Te. Note that here we have adjusted the scaling factor of Te to be three times that of Fe for the Te layer to demonstrate its features around the Fermi surface more clearly. Both Fe and Te exhibit states crossing the Fermi surface that give rise to the small but nonzero contribution in PDOS (Fig. 6(g)). Also, in the calculated PDOS, there are local maxima at around −1.0 eV and +0.7 in the Fe layer (marked by red arrows in Fig. 6(g)) as a result of rather flat dispersion in Fe bands. These PDOS maxima, as well as the non-zero PDOS across the Fermi surface, are able to find their qualitative correspondence in the tunneling d*I*/d*U* spectrum (Fig. 6(h)).

To gain insights, the magnetic properties have been calculated for the α-FeTe monolayer on Bi_2Te_3, where the in-plane and out-of-plane magnetic moments are 2.97 μ_B and 1.67 μ_B, respectively, and together give a total moment of 3.41 μ_B, almost all from the Fe atoms. This indicates the ferromagnetism in α-FeTe monolayer/Bi_2Te_3. Such magnetization is distinct from the bicollinear antiferromagnetism observed in the β-FeTe monolayer/Bi_2Te_3, which has been studied much more extensively than its α-FeTe counterpart.

The magnetization can be further supported from the spin-dependent band calculation results as shown in Fig. 7(a) and (b) for Fe projected to s_z spin-up $s_{z,\uparrow}$ (red) and spin-down $s_{z,\downarrow}$ (blue). The projection is chosen specifically in the z-direction so that it can compare more closely with the future spin-polarized STS (SP-STS) measurement. The projection is essentially the same self-consistent DFT calculation as in the previous section but we now project the band information to the spin degree of freedom for Fe. From Fig. 7(a), the $s_{z,\uparrow}$ dominates in a larger energy range (−6 to −2 eV), not only that there is significantly more $s_{z,\uparrow}$ contribution in this energy range but a few especially strong $s_{z,\uparrow}$ projections at around −3.0 eV and −4.5 eV. However, in the vicinity of the Fermi surface (Fig. 7(b)), the situation reverses, *i.e.*, $s_{z,\downarrow}$ disperses dominantly nearby Fermi energy (−1 to +1 eV). We also plot the corresponding PDOS (Fig. 7(c)) in that energy range, focusing especially around $\bar{\Gamma}$. Indeed, we observe that local maxima of PDOS, *e.g.*, at −1.0 and +0.7 in Fig. 6(g), are mainly contributed by $s_{z,\downarrow}$, which gives roughly three times the contribution of $s_{z,\uparrow}$. In addition, we also perform the orbital projection of calculated PDOS in order to analyze the important role of the Fe 3d orbitals in the magnetic properties (Fig. 7(d)). Here we find that the contribution of out-of-plane orbitals (sum of d_{xz}, d_{yz} and d_{z^2}) overwhelms the in-plane orbitals (d_{xy} and $d_{x^2-y^2}$), explaining that the enhanced PDOS in Fig. 6(h) mostly comes from out-of-plane Fe 3d orbitals.

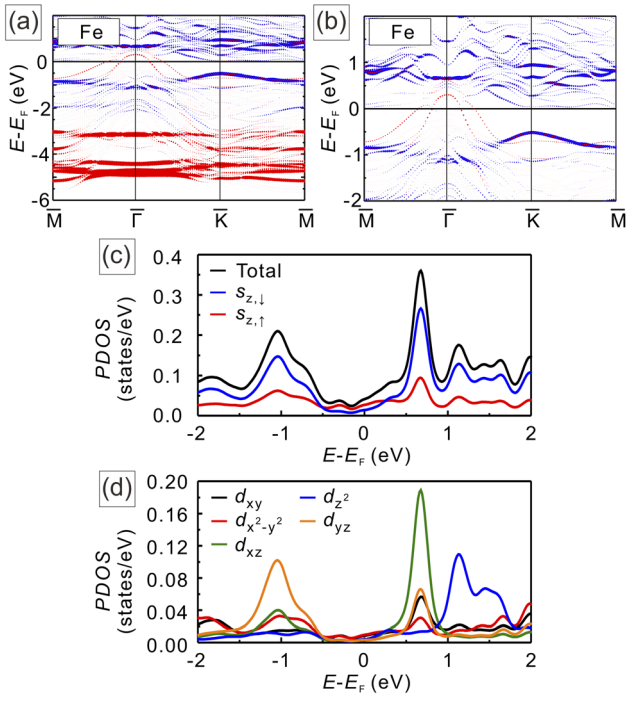

Fig. 7 (a) Fe projected band structure in s_z for spin-up ($s_{z,\uparrow}$, red) and spin-down ($s_{z,\downarrow}$, blue) from −6 to 2 eV. Overall the $s_{z,\uparrow}$ projection dominates at around −3.0 eV and −4.5 eV. (b) The zoom-in of (a) in the vicinity of the Fermi surface (−2 to 2 eV) showing that the $s_{z,\downarrow}$ turns out to play a more important role in this energy range. (c) The corresponding PDOS plot for (b) clearly shows the significance of $s_{z,\downarrow}$ in the local maxima peaks. (d) The orbital projected PDOS in the same energy range showing that the contribution of out-of-plane orbitals dominates over in-plane orbitals.

4 Conclusion

In summary, we have grown and characterized the α-FeTe monolayer on 3D TI Bi_2Te_3 by exploiting STM/STS combined with DFT. Through depositing Fe onto an *in situ* cleaved Bi_2Te_3 surface at RT followed by post-annealing to 560 K, α-FeTe with an atomic lattice constant of 4.0 ± 0.1 Å has been successfully fabricated. Although the crystalline orientation symmetry of the α-FeTe monolayer is identical to the bulk Bi_2Te_3 substrate, a moiré pattern appears with a periodicity of 6.0 ± 0.1 nm and corresponds to a $p(15 \times 15)$ superlattice as a consequence of lattice mismatch and interfacial structure gap formation. According to spin-dependent band structures, out-of-plane Fe atomic orbitals, *e.g.*, $3d_{yz}$ (−1.0 eV) and $3d_{xz}$ (+0.7 eV), have major contribution to the enhanced PDOS at about −0.8 eV and +1.4 eV in the tunneling dI/dU spectra on α-FeTe/Bi_2Te_3. Furthermore, the $s_{z,\downarrow}$ contribution distributes mostly around the Fermi level while the $s_{z,\uparrow}$ contribution buries deep in the Fermi sea. The imbalance of up- and down-spins in all directions results in a net magnetic moment of about 3.41 μ_B in Fe atoms, playing an indispensable role in developing possible magnetic order in the α-FeTe monolayer. Given the systematic growth studies of α-FeTe/Bi_2Te_3, it offers an opportunity not only to explore intriguing magnetic properties and superconducting phenomena, but also to offer a comparison with β-FeTe/Bi_2Te_3.

Data availability

The data supporting this article can be accessed here: **https://doi.org/10.17605/OSF.IO/J79PK**.

Author contributions

Y. H. L., G. Y. C., H. C. L., N. K., C. J. C. and P. J. H. conducted the STM/STS experiments and data analyses; D. A. L. synthesized the Bi_2Te_3 single crystal; Y. H. C., J. A. L., A. H. M. and J. J. S. performed the DFT calculations. All authors contributed to the discussion of the manuscript.

Conflicts of interest

The authors declare no competing financial interests.

Acknowledgements

P. J. H. acknowledges support from the National Science and Technology Council of Taiwan under grant no. NSTC-112-2636-M-007-006 and NSTC-112-2112-M-007-037, Ministry of Science and Technology of Taiwan under grant no. MOST-111-2636-M-007-007 and MOST-110-2636-M-007-006, and center for quantum science and technology from the featured areas research center program within the framework of the higher education sprout project by the Ministry of Education (MOE) in Taiwan. J.-J. S. acknowledges the support from the Ministry of Science and Technology, Taiwan MOST-112-2112-M-A49-039, the Center for Theoretical and Computational Physics (CTCP) of National Yang Ming Chiao Tung University (NYCU) and the generous computing resources from the National Center for High-performance Computing.

References

1 A. Subedi, L. Zhang, D. J. Singh and M. H. Du, *Phys. Rev. B:Condens. Matter Mater. Phys.*, 2008, **78**, 134514.
2 J. Paglione and R. L. Greene, *Nat. Phys.*, 2010, **6**, 645–658.
3 G. R. Stewart, *Rev. Mod. Phys.*, 2011, **83**, 1589–1652.
4 X. Liu, L. Zhao, S. He, J. He, D. Liu, D. Mou, B. Shen, Y. Hu, J. Huang and X. J. Zhou, *J. Phys.: Condens. Matter*, 2015, **27**, 183201.
5 P. Zhang, K. Yaji, T. Hashimoto, Y. Ota, T. Kondo, K. Okazaki, Z. Wang, J. Wen, G. D. Gu, H. Ding and S. Shin, *Science*, 2018, **360**, 182–186.
6 F.-C. Hsu, J.-Y. Luo, K.-W. Yeh, T.-K. Chen, T.-W. Huang, P. M. Wu, Y.-C. Lee, Y.-L. Huang, Y.-Y. Chu, D.-C. Yan and M.-K. Wu, *Proc. Natl. Acad. Sci. U. S. A.*, 2008, **105**, 14262–14264.
7 J. J. Seo, B. Y. Kim, B. S. Kim, J. M. Jeong, J. K. andOk, J. S. Kim, J. Denlinger, S.-K. Mo, C. Kim and Y. K. Kim, *Nat. Commun.*, 2016, **7**, 11116.
8 Y. Meng, X. Xing, X. Yi, B. Li, N. Zhou, M. Li, Y. Zhang, W. Wei, J. Feng, K. Terashima, Y. Takano, Y. Sun and Z. Shi, *Phys. Rev. B*, 2022, **105**, 134506.
9 Q.-Y. Wang, Z. Li, W.-H. Zhang, Z.-C. Zhang, J.-S. Zhang, W. Li, H. Ding, Y.-B. Ou, P. Deng, K. Chang, J. Wen, C.-L. Song, K. He, J.-F. Jia, S.-H. Ji, Y. Wang, L. Wang, X. Chen, X. Ma and Q.-K. Xue, *Chin. Phys. Lett.*, 2012, **29**, 037402.
10 W.-H. Zhang, Y. Sun, J.-S. Zhang, F.-S. Li, M.-H. Guo, Y.-F. Zhao, H.-M. Zhang, J.-P. Peng, Y. Xing, H.-C. Wang, F. Takeshi, H. Akihiko, Z. Li, H. Ding, C.-J. Tang, M. Wang, Q.-Y. Wang, K. He, S.-H. Ji, X. Chen, J.-F. Wang, Z.-C. Xia, L. Li, Y.-Y. Wang, J. Wang, L.-L. Wang, M.-W. Chen, Q.-K. Xue and X.-C. Ma, *Chin. Phys. Lett.*, 2014, **31**, 017401.
11 L. Z. Deng, B. Lv, Z. Wu, Y. Y. Xue, W. H. Zhang, F. S. Li, L. L. Wang, X. C. Ma, Q. K. Xue and C. W. Chu, *Phys. Rev. B:Condens. Matter Mater. Phys.*, 2014, **90**, 214513.
12 Y. Sun, W. Zhang, Y. Xing, F. Li, Y. Zhao, Z. Xia, L. Wang, X. Ma, Q.-K. Xue and J. Wang, *Sci. Rep.*, 2014, **4**, 6040.
13 J.-F. Ge, Z.-L. Liu, C. Liu, C.-L. Gao, D. Qian, Q.-K. Xue, Y. Liu and J.-F. Jia, *Nat. Mater.*, 2015, **14**, 285–289.
14 R. Peng, H. Xu, S. Tan, H. Cao, M. Xia, X. Shen, Z. Huang, C. Wen, Q. Song, T. Zhang, B. P. Xie, X. G. Gong and D. L. Feng, *Nat. Commun.*, 2014, **5**, 5044.
15 X. Fan, W. Cui, Y. Yuan, Q.-K. Xue and W. Li, *Phys. Rev. B*, 2022, **106**, 024517.
16 Y. Song, Z. Chen, Q. Zhang, H. Xu, X. Lou, X. Chen, X. Xu, X. Zhu, R. Tao, T. Yu, H. Ru, Y. Wang, T. Zhang, J. Guo, L. Gu, Y. Xie, R. Peng and D. Feng, *Nat. Commun.*, 2021, **12**, 5926.
17 F. Li, H. Ding, C. Tang, J. Peng, Q. Zhang, W. Zhang, G. Zhou, D. Zhang, C.-L. Song, K. He, S. Ji, X. Chen, L. Gu, L. Wang, X.-C. Ma and Q.-K. Xue, *Phys. Rev. B:Condens. Matter Mater. Phys.*, 2015, **91**, 220503.
18 X.-L. Peng, Y. Li, X.-X. Wu, H.-B. Deng, X. Shi, W.-H. Fan, M. Li, Y.-B. Huang, T. Qian, P. Richard, J.-P. Hu, S.-H. Pan, H.-Q. Mao, Y.-J. Sun and H. Ding, *Phys. Rev. B*, 2019, **100**, 155134.
19 Z. Zhang, M. Cai, R. Li, F. Meng, Q. Zhang, L. Gu, Z. Ye, G. Xu, Y.-S. Fu and W. Zhang, *Phys. Rev. Mater.*, 2020, **4**, 125003.
20 L. Kang, C. Ye, X. Zhao, X. Zhou, J. Hu, Q. Li, D. Liu, C. M. Das, J. Yang, D. Hu, J. Chen, X. Cao, Y. Zhang, M. Xu, J. Di, D. Tian, P. Song, G. Kutty, Q. Zeng, Q. Fu, Y. Deng, J. Zhou, A. Ariando, F. Miao, G. Hong, Y. Huang, S. J. Pennycook, K.-T. Yong, W. Ji, X. Renshaw Wang and Z. Liu, *Nat. Commun.*, 2020, **11**, 3729.
21 M. Cheng, X. Zhao, Y. Zeng, P. Wang, Y. Wang, T. Wang, S. J. Pennycook, J. He and J. Shi, *ACS Nano*, 2021, **15**, 19089–19097.
22 Q. L. He, H. Liu, M. He, Y. H. Lai, H. He, G. Wang, K. T. Law, R. Lortz, J. Wang and I. K. Sou, *Nat. Commun.*, 2014, **5**, 4247.
23 H. T. He, G. Wang, H. C. Liu, T. Zhang, K. T. Law, I. K. Sou and J. N. Wang, *Solid State Commun.*, 2014, **195**, 35–38.
24 S. Manna, A. Kamlapure, L. Cornils, T. Hänke, E. Hedegaard, M. Bremholm, B. Iversen, P. Hofmann, J. Wiebe and R. Wiesendanger, *Nat. Commun.*, 2017, **8**, 14074.
25 M. Enayat, Z. Sun, U. R. Singh, R. Aluru, S. Schmaus, A. Yaresko, Y. Liu, C. Lin, V. Tsurkan, A. Loidl, J. Deisenhofer and P. Wahl, *Science*, 2014, **345**, 653–656.
26 L. Fu and C. L. Kane, *Phys. Rev. Lett.*, 2008, **100**, 096407.
27 X.-L. Qi, T. L. Hughes, S. Raghu and S.-C. Zhang, *Phys. Rev. Lett.*, 2009, **102**, 187001.
28 M.-X. Wang, C. Liu, J.-P. Xu, F. Yang, L. Miao, M.-Y. Yao, C. L. Gao, C. Shen, X. Ma, X. Chen, Z.-A. Xu, Y. Liu, S.-C. Zhang, D. Qian, J.-F. Jia and Q.-K. Xue, *Science*, 2012, **336**, 52–55.
29 J. Alicea, *Rep. Prog. Phys.*, 2012, **75**, 076501.
30 C. W. J. Beenakker, *Annu. Rep. Condens. Matter Phys.*, 2013, **4**, 113–136.
31 D. Aasen, M. Hell, R. V. Mishmash, A. Higginbotham, J. Danon, M. Leijnse, T. S. Jespersen, J. A. Folk, C. M. Marcus, K. Flensberg and J. Alicea, *Phys. Rev. X*, 2016, **6**, 031016.
32 J. Shen, R. Skomski, M. Klaua, H. Jenniches, S. Sundar Manoharan and J. Kirschner, *J. Appl. Phys.*, 1997, **81**, 3901–3903.

33 S.-H. Phark, J. A. Fischer, M. Corbetta, D. Sander, K. Nakamura and J. Kirschner, *Nat. Commun.*, 2014, **5**, 5183.
34 L. Gerhard, T. K. Yamada, T. Balashov, A. F. Takács, R. J. H. Wesselink, M. Däne, M. Fechner, S. Ostanin, A. Ernst, I. Mertig and W. Wulfhekel, *Nat. Nanotech.*, 2010, **5**, 792–797.
35 A. K. Kaveev, S. M. Suturin, V. A. Golyashov, K. A. Kokh, S. V. Eremeev, D. A. Estyunin, A. M. Shikin, A. V. Okotrub, A. N. Lavrov, E. F. Schwier and O. E. Tereshchenko, *Phys. Rev. Mater.*, 2021, **5**, 124204.
36 T. Hänke, U. R. Singh, L. Cornils, S. Manna, A. Kamlapure, M. Bremholm, E. M. J. Hedegaard, B. B. Iversen, P. Hofmann, J. Hu, *et al.*, *Nat. Commun.*, 2017, **8**, 13939.
37 F. Arnold, J. Warmuth, M. Michiardi, J. Fikáček, M. Bianchi, J. Hu, Z. Mao, J. Miwa, U. R. Singh, M. Bremholm, R. Wiesendanger, J. Honolka, T. Wehling, J. Wiebe and P. Hofmann, *J. Phys.: Condens. Matter*, 2018, **30**, 065502.
38 V. Tkáč, S. Vorobiov, P. Baloh, M. Vondráček, G. Springholz, K. Carva, P. Szabó, P. Hofmann and J. Honolka, *npj 2D Mater. Appl.*, 2024, **8**, 52.
39 Q. M. Chen, F. Z. Cui, Y. D. Fan and H. D. Li, *J. Appl. Phys.*, 1988, **63**, 2452.
40 C. G. Ünlü, Z.-A. Li, M. Acet and M. Farle, *Cryst. Res. Technol.*, 2016, **51**, 333.
41 Z. B. Liang, Y. C. Jiang, X. Gong and H. R. Gong, *J. Phys.: Condens. Matter*, 2022, **34**, 025901.
42 S. Li, C. de la Cruz, Q. Huang, Y. Chen, J. W. Lynn, J. Hu, Y.-L. Huang, F.-C. Hsu, K.-W. Yeh, M.-K. Wu and P. Dai, *Phys. Rev. B:Condens. Matter Mater. Phys.*, 2009, **79**, 054503.
43 A. Sugimoto, R. Ukita and T. Ekino, *Phys. Proc.*, 2013, **45**, 85–88.
44 T. Machida, K. Kogure, T. Kato, H. Nakamura, H. Takeya, T. Mochiku, S. Ooi, Y. Mizuguchi, Y. Takano, K. Hirata, *et al.*, *J. Phys. Soc. Jpn.*, 2012, **81**, 074714.
45 R. W. G. Wyckoff, *Crystal Structures 2nd edn*, 1963, vol. 1, p. 124.